Available online at www.sciencedirect.com

SciVerse ScienceDirect

Ceramics International 38 (2012) 5683–5690

CERAMICS INTERNATIONAL

www.elsevier.com/locate/ceramint

Optical and structural properties of X-doped (X = Mn, Mg, and Zn) PZT nanoparticles by Kramers–Kronig and size strain plot methods

Gh.H. Khorrami [a], A. Khorsand Zak [a,*], A. Kompany [a], Ramin yousefi [b]

[a] *Materials and Electroceramics Lab., Department of Physics, Faculty of Science, Ferdowsi University of Mashhad, Iran*
[b] *Department of Physics, Masjed-Soleiman Branch, Islamic Azad University (I.A.U), Masjed-Soleiman, Iran*

Received 7 March 2012; received in revised form 3 April 2012; accepted 3 April 2012
Available online 12 April 2012

Abstract

Pure and X doped (X = Mg, Mn, and Zn) lead zirconate titanate nanoparticles (PZT-NPs) were synthesized using sol-combustion method. The xerogel was calcined at temperature of 700 °C for 2 h. The structure of the prepared powders is characterized using X-ray diffraction (XRD) and Fourier transform infrared (FTIR) spectroscopy. The XRD results show that the PZT-NPs are formed in perovskite structure with rhombohedral phase. In addition, a small shift was detected in XRD patterns of doped PZT-NPs. Also, the XRD results were analyzed using size strain plot (SSP) to calculate the lattice strain of the prepared samples, which revealed that the lattice strain depends on the different ionic radii of the dopants. To have a better understanding of the optical properties of the pure and doped PZT-NPs, the obtained FTIR spectra were analyzed using Kramers–Kronig method. The results show that there are certain relations between the optical parameters and the wavelength of the incident beam as well as the optical modes. Also, the value of the pure and doped PZT-NPs optical band gaps were estimated using ultra violet and visible (UV–vis) spectroscopy. It was found that the optical properties of the doped samples depend strongly on dopants.

Keywords: B. Optical properties; D. PZT; XRD; Lattice strain

1. Introduction

In the past few decades, piezoelectric materials because of their various interesting properties have been extensively used in different branches of science and technology including medicine, electronics, military, and oil industries. Lead zirconate titanate (PZT) is an important class of piezoelectric and ferroelectric materials having unique properties [1], PZT is used for fabricating many electronic and optoelectronic devices such as sensors [2], capacitors [3], random access memories (RAM) [4], optical modulators and waveguides [5]. It has been found that the nano structure of PZTs have more interesting properties, so different physical and chemical methods have been developed to prepare of nano-sized PZT powders such as, sol–gel [6,7], sol-combustion [8], hydrothermal [9], solvothermal [10], precipitation [11], and solid state reactions [12].

Many factors such as solvent [13] and dopant [14] can affect the optical properties of PZT. Therefore, they can be used to control the properties of the PZTs. In addition, the crystal defects affect the optical properties of these materials. Furthermore, doping causes some strain in crystal lattice, which changes the optical and physical properties of the materials [15]. Lattice strain is a measure of the distribution of lattice constants arising from crystal imperfections, such as lattice dislocations due to different ionic radii of dopants comparing to the matrix ions. Both lattice strain (due to the dopant) and crystallite size affect the 2θ peak position, intensity, and broadening of the Bragg peaks, Fig. 1. The crystallite size derived from the peak widths varies as $1/\cos\theta$, whereas strain varies as $\tan\theta$ [16]. There are some methods to calculate the strain and the crystallite size considering the lattice strain [6]. Size strain plot (SSP) method is used to calculate the crystallite size and its strain [16]. In this method, it is ‘‘crystallite size’’ profile is described by a Lorentzian function and the ‘‘strain profile’’ by a Gaussian function [17]. Fourier transform infrared (FTIR) spectroscopy is a suitable technique to study the optical properties of both inorganic and organic materials in which

---

[*] Corresponding author.
E-mail address: alikhorsandzak@gmail.com (A. Khorsand Zak).

0272-8842/$36.00 © 2012 Elsevier Ltd and Techna Group S.r.l. All rights reserved.
http://dx.doi.org/10.1016/j.ceramint.2012.04.012

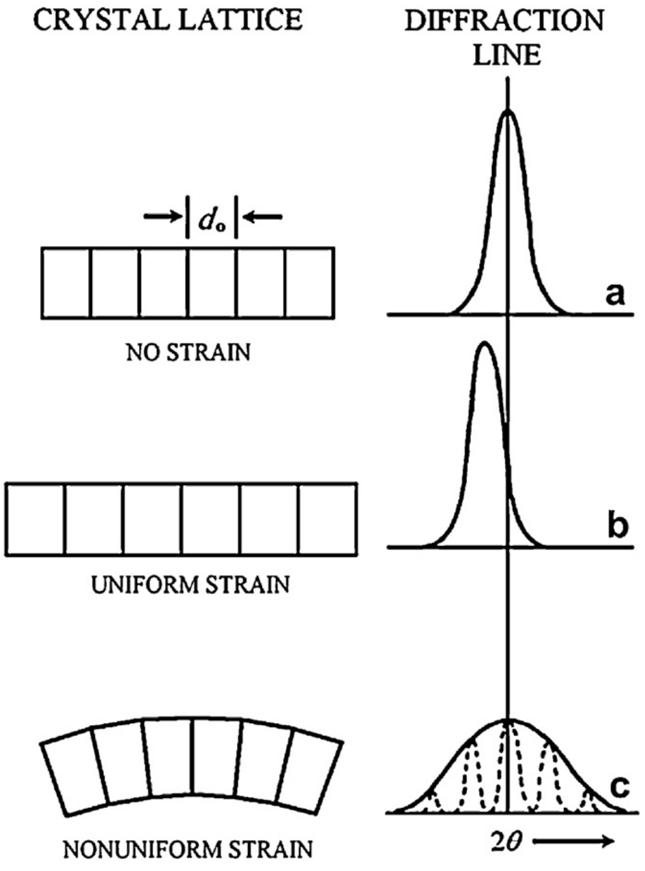

Fig. 1. Effect of uniform and nonuniform strain on peak broadening XRD patterns.

some mathematical methods are used for the analysis of obtained IR spectra. The most famous mathematical method that has been used widely is Kramers–Kronig (K–K).

In this work, the pure and X-doped PZT-NPs (X = Mn, Mg, and Zn) were prepared by modified sol-combustion method. These dopants were chosen because of their different ionic radii comparing to Ti, to investigate the effect of occurred strain on the optical and structural properties of PZT-NPs, (r_{Zn} and $r_{Mg} > r_{Ti} > r_{Mn}$) by SSP and K–K, respectively. In addition, the values of the optical band gap of the samples have been estimated using UV–vis spectra.

2. Experimental

To prepare pure PZT-NPs, the starting materials were chosen according to $Pb(Zr_{0.52},Ti_{0.48})O_3$ compound. First, a solution of citric and nitric acids were prepared, by dissolving citric acid in minimum water needed and then adding the nitric acid to the citric acid solution at room temperature. After that, the titanium iso-propoxide was added to the solution and stirred to get a clear solution. The amounts of the acids used were selected as below:

$$\frac{\text{Citric-acid}}{\text{Metal-cation}} = 2.5 \quad \text{and} \quad \frac{\text{Citric-acid}}{\text{Nitric-acid}} = 1.3$$

At the same time, lead nitrate and zirconium oxynitrate were dissolved in minimum water at 50 °C, separately. Then, the lead nitrate and zirconium oxynitrate solutions were added to the titanium isopropoxide solution, gently. pH of the obtained solution was adjusted at 7 by adding ammonia solution following refluxing of the prepared solution at 100 °C for 2 h. The refluxed solution was dried on a hot plate using nitrate acid as fuel for the combustion process. After the calcinations of produced xerogel at 700 °C for 2 h in air atmosphere a yellow powders was obtained. The processes for preparing PZT-NPs doped with X (X = Mg, Mn, and Zn) were the same as pure PZT-NPs, according to $Pb(Zr_{0.52},Ti_{0.43}X_{0.05})O_3$ compounds, respectively.

The prepared pure and doped powders were characterized by X-ray diffraction (XRD, Philips, X'pert, Cu Kα), Fourier transform infrared (FTIR) spectroscopy, and field emission scanning electron microscopy (FESEM).

3. Results and discussion

3.1. X-ray diffraction analysis

The XRD patterns of the pure and doped PZT compounds are shown in Fig. 2. All the peaks are related to rhombohedral phase and prove the formation of the PZT in perovskite structure after calcination process at 700 °C for 2 h. No extra peaks, related to the dopants, are detected. The crystallite size of the powders are estimated by Scherrer's equation using (1 1 0) peak. The crystallite size of the pure and doped PZT is presented in Table 1. A small shift is observed for (1 1 0) peak of the doped samples, in which Ti^{+4} ions are substituted (ionic radius = 0.61 Å) by Mn^{2+} (ionic radius = 0.46 Å), Zn^{2+} (ionic radius = 0.74 Å), and Mg^{2+} (ionic radius = 0.72 Å), comparing to the pure PZT, Fig. 3. Also, it can be seen in the patterns that the intensity of doped samples peaks are less than that for the pure sample. These peak shifts and the intensity changes are attributed to the presence of both uniform and non-uniform

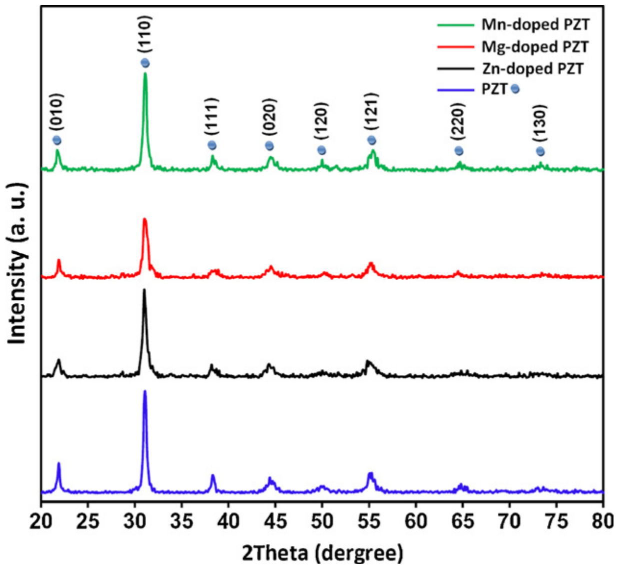

Fig. 2. X-ray diffraction patterns of the pure and Zn, Mg, and Mn doped PZT-NPs.

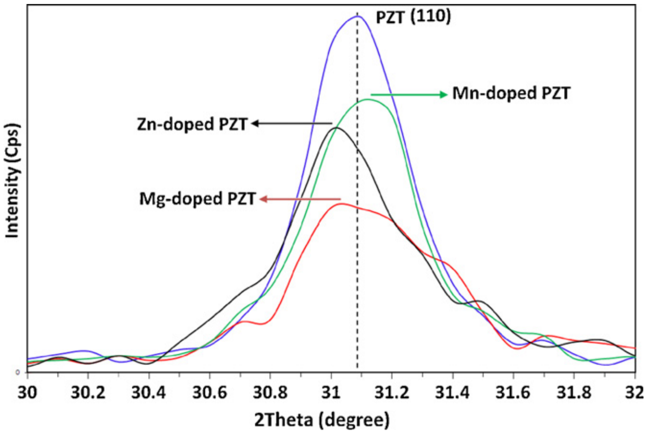

Fig. 3. (1 1 0) crystal surface X-ray diffraction patterns of pure and Zn, Mg, and Mn doped PZT-NPs.

Table 1
Size strain plot analysis results of pure and doped PZT-NPs.

Compound	Crystallite size (D) using Scherrer equation (nm)	Size strain plot	
		Crystallite size (D) (nm)	Strain (ε) $\times 10^{-3}$
PZT	21	94	0.6
Zn-doped PZT	18	90	1.73
Mg-doped PZT	14	65	7.07
Mn-doped PZT	20	100	1

strains in the doped compound lattices due to the different ionic radii of the dopants comparing to Ti ions [18]. For Mn^{2+} the shift is to higher angles; whereas substitution of Zn^{2+} and Mg^{2+} result in the shift to lower angles. As mentioned above $r_{Mn} < r_{Ti}$, then the lattice is shrinked leading to the decrease of the d spacing of the planes. Therefore, the XRD pattern of the corresponding planes to this d spacing will shift to higher angles as expected from Braggs law. Since $r_{(Zn \text{ and } Mg)} > r_{Ti}$, the lattice is expanded by substitution of Ti ions by Zn and Mg ions, therefore, the corresponding XRD patterns peak is shifted to lower angles, Fig. 4. The d space between adjacent $(h\,k\,l)$ planes can be calculated from Bragg equation. The lattice constants a, b, c, the interplanar angle, the angle φ between the plane $(h_1\,k_1\,l_1)$, and the plane $(h_2\,k_2\,l_2)$, and the cell volumes can be calculated from the Lattice Geometry equations [18]. The calculated lattice parameters of PZT powders doped with different elements of Zn, Mg, and Zn are summarized in Table 2.

3.2. XRD data analysis using size strain plot (SSP)

The peak broadening observed in XRD patterns can be evaluated in terms of crystallite size and lattice strain due to Ti^{4+} substituted by Zn^{2+}, Mg^{2+}, and Mn^{2+} ions in PZT structure. In the case of isotropic line broadening, a good evaluation of the crystal-strain parameters can be obtained by considering the average ‘‘size–strain plot’’ (SSP), which has the advantage of giving less weight to data obtained from reflections at high angles, in which the accuracy is usually lower comparing to the other methods [6]. Accordingly, we have:

$$(d_{hkl}\beta_{hkl}\cos\theta)^2 = \frac{K}{D}(d_{hkl}^2\beta_{hkl}\cos\theta) + \left(\frac{\varepsilon}{2}\right)^2 \tag{1}$$

where K is a constant that depends on the shape of the particles. For spherical shape particles K is $^3/_4$. In Fig. 5, the term $(d_{hkl}\beta_{hkl}\cos\theta)^2$ is plotted with respect to $(d_{hkl}{}^2\beta_{hkl}\cos\theta)$ for all the peak orientations of pure and doped PZT-NPs with the rhombohedral phase from $2\theta = 20°$ to $2\theta = 80°$. In this case, the crystallite size and the lattice strain are obtained from the slope of the linearly fitted data and the root of the y-intercept, respectively. The results are presented in Table 1. As mentioned above, the broadening of (1 1 0) peak in Fig. 3 for doped samples can be related to both the crystallite size and non-uniform lattice strain. Our results show that, the maximum peak broadening and strain are observed in Mg doped PZT-NPs. It means that the strain increase is the major reason for peak broadening in Mg doped PZT-NPs, while the crystallite size is

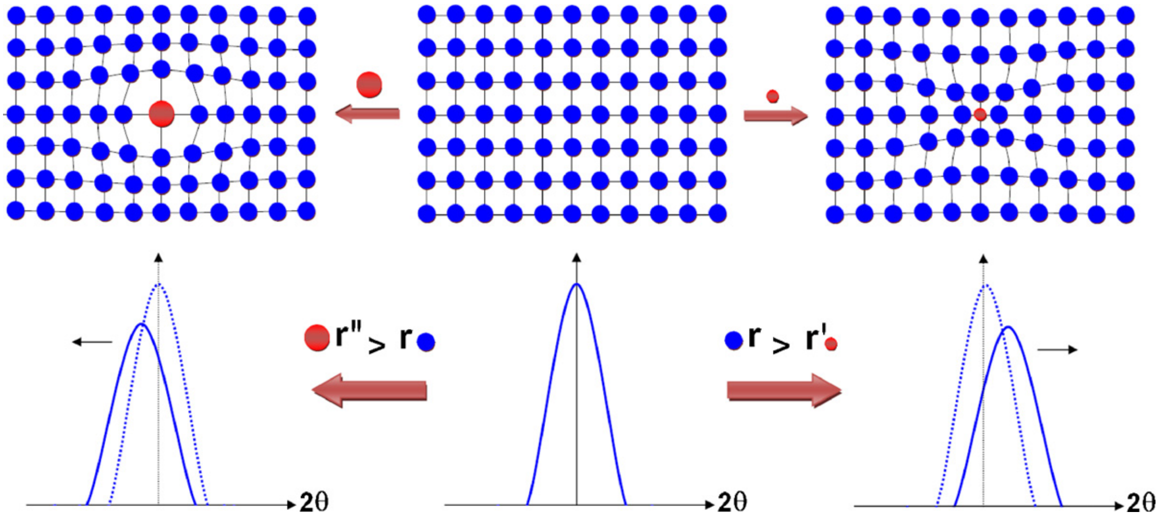

Fig. 4. Effect of doping with different ionic radii on lattice structure of materials.

Table 2
Geometric structural parameters of pure and doped PZT-NPs.

Compound	$2\theta \pm 0.1$	d_{hkl} (nm) ± 0.0001	*h k l*	Structure	Lattice parameter (nm) ± 0.0001 ± 0.01	$V \pm 0.01$	$\cos\varphi \pm 0.0001$
PZT	21.9	0.4064	0 1 0	Rhombohedral	$a = b = c = 0.4064$	67.12	0.7072
	31.1	0.2874	1 1 0		$\alpha = 90.01$		
Zn-doped PZT	21.8	0.4067	0 1 0	Rhombohedral	$a = b = c = 0.4032$	65.56	0.7220
	31.0	0.2879	1 1 0		$\alpha = 90.14$		
Mg-doped PZT	21.9	0.4056	0 1 0	Rhombohedral	$a = b = c = 0.3999$	63.97	0.7317
	30.1	0.2874	1 1 0		$\alpha = 90.23$		
Mn-doped PZT	21.8	0.4072	0 1 0	Rhombohedral	$a = b = c = 0.4136$	70.74	0.6811
	31.1	0.2873	1 1 0		$\alpha = 89.75$		

the major reason for peak broadening for Zn doped PZT-NPs XRD pattern. The small strain in the pure PZT can be related to the lattice defects due to oxygen vacancies and other source of defects.

3.3. *Optical properties of the pure and doped PZT-NPs*

3.3.1. *FTIR*

The room temperature transmittance of pure and doped PZT-NPs was investigated by Fourier transform infrared (FTIR) spectroscopy in the range of 280–4000 cm $^{-1}$ and the results are presented in Fig. 6. As expected for perovskite structures, a broad band with minimum transmittance between 530 and 540 cm^{-1} and another one with minimum transmittance in the range of 327–346 cm^{-1} were observed in each spectrum. According to the literature, these two absorption bands are attributed to MO_6 (M = Zr and Ti) stretching and bending in the octahedral normal modes, respectively [13]. The stretching normal vibration occurs at higher frequency, ν_1 and the bending normal vibration at lower frequency, ν_2 [19]. The minimum of the transmittance shift occurs by substitution of Ti with Mn and Zn, due to the difference in their ionic radii and weights. There are two other vibration modes (ν_3 and ν_4), which are related to vibrations of Pb–TiO_3/ZrO_3 bonds, but these modes occur below the available experimental frequency range (280–4000 cm^{-1}) used in this experiment and are not seen in the spectra. The results are summarized in Table 3.

3.3.2. *Theory of K–K method*

The K–K method was used to evaluate the optical constants of pure and doped PZT-NPs prepared by the sol-combustion method using FTIR transmittance spectra data. Absorption is characterized by a decrease in transmitted light intensity through the sample. The quantity used to discuss the absorption, as a function of the wavenumber, is the transmittance (*T*), which is the ratio of the intensity of the light transmitted through the sample (*I*) to the incident light intensity (I_o). Transmittance is usually given by the more common percent transmittance (*T*%)

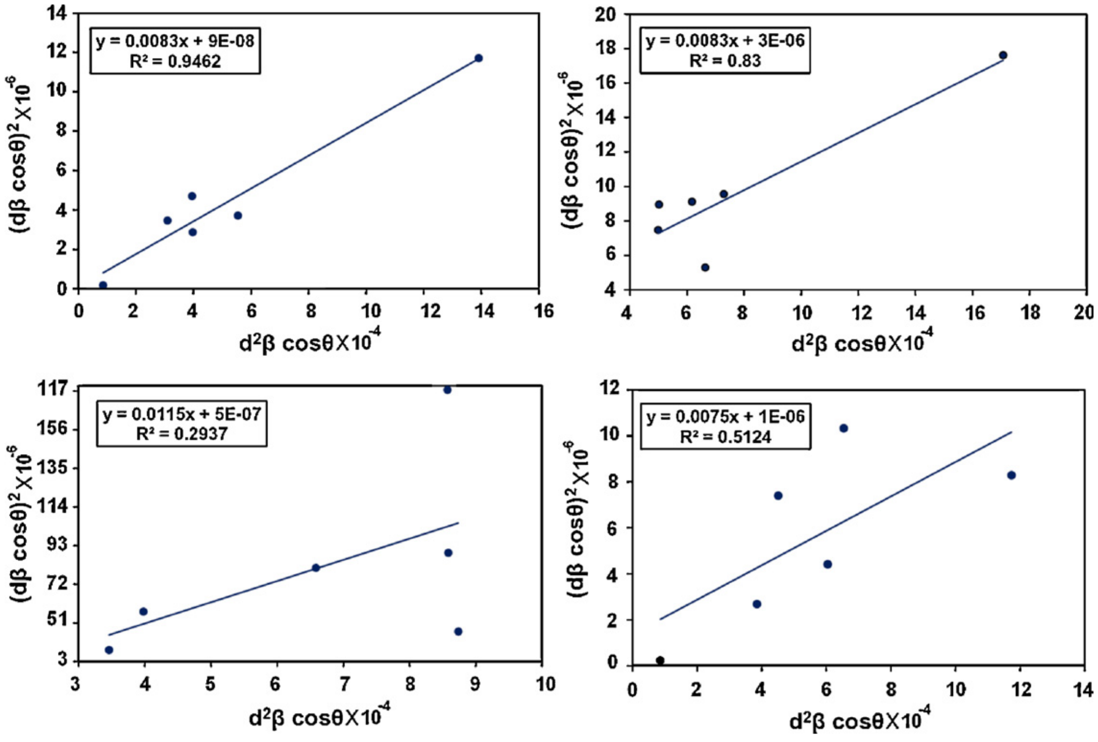

Fig. 5. SSP plot of (a) pure PZT-NPs, (b) Zn doped-PZT-NPs, (c) Mg-doped PZT-NPs, and (d) Mn-doped PZT-NPs.

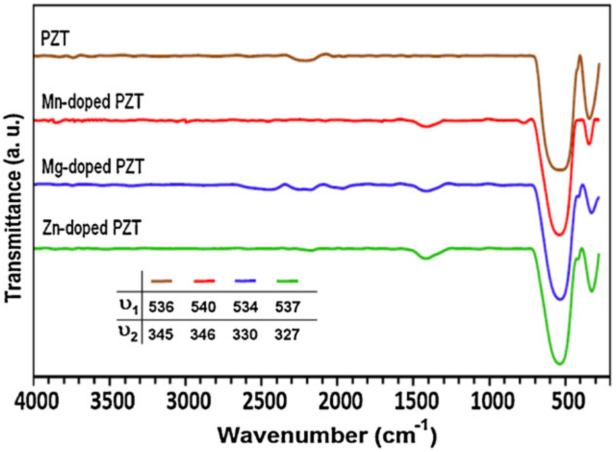

Fig. 6. FTIR transmittance traces of the pure and doped PZT-NPs.

by $T\% = 100T$. The absorption (A) is defined as $\log_{10}(1/T)$, according to Lambert's principle [20]

$$A(\omega) = \log_{10}\frac{I_0}{I} = \log_{10}\frac{1}{T(\omega)} = 2 - \log(T(\omega)\%) \tag{2}$$

$$\Rightarrow R(\omega) = 100 - [T(\omega) + A(\omega)] \tag{3}$$

where $R(\omega)$ is the reflectance at a particular wavenumber. The refractive index N is the most widely physical quantity used in optical design. Generally, it is a complex quantity given as:

$$\tilde{N}(\omega) = n(\omega) + ik(\omega) \tag{4}$$

where $n(\omega)$ and $k(\omega)$ are the real and imaginary parts of the complex refractive index, respectively obtained from the following equations

$$n(\omega) = \frac{1 - R(\omega)}{1 + R(\omega) - 2\sqrt{R(\omega)}\cos\varphi(\omega)} \tag{5}$$

$$k(\omega) = \frac{2\sqrt{R(\omega)}\sin\varphi(\omega)}{1 + R(\omega) - 2\sqrt{R(\omega)}\cos\varphi(\omega)} \tag{6}$$

Table 3
Longitudinal and transverse optical phonon modes (LO and TO) of pure and PZT-NPs.

	PZT	Zn-doped PZT	Mg-doped PZT	Mn-doped PZT
ν_1	536	537	534	540
ν_2	345	333	330	346
Longitudinal (LO)	679	673	670	676
Transverse (TO)	497	496	493	498

where $R(\omega)$ is the reflectance and $\varphi(\omega)$ is the phase change between the incident and reflected signals for a particular wavenumber ω. This phase change can be derived from K–K dispersion relation [21]

$$\varphi(\omega) = \frac{-\omega}{\pi}\int_0^{\infty}\frac{\ln R(\omega') - \ln R(\omega)}{\omega'^2 - \omega^2}d\omega' \tag{7}$$

Also, $\varphi(\omega)$ can be obtained from Fourier transform of K–K dispersion relation [22]. The Fourier transform of K–K was chosen to avoid the singularity that may happen in the integral.

$$\varphi(\omega_j) = \frac{4\omega_j}{\pi} \times \Delta\omega \times \sum_i \frac{\ln(\sqrt{R(\omega)})}{\omega_i^2 - \omega_j^2} \tag{8}$$

where $\Delta\omega = \omega_{i+1} - \omega_i$ and if j is an odd number then $i = 2, 4, 6, \ldots, j-1, j+1, \ldots$ but, if j is an even number $i = 1, 3, 5, \ldots, j-1, j+1, \ldots$

The dielectric function is the square of the refractive index. Therefore, the real and imaginary parts of the complex dielectric function can be written as:

$$\tilde{\varepsilon}(\omega) = [\tilde{N}(\omega)]^2 = [n(\omega) + ik(\omega)]^2 \tag{9}$$

$$\Rightarrow \varepsilon'(\omega) + i\varepsilon''(\omega) = n^2(\omega) - k^2(\omega) + 2in(\omega)k(\omega) \tag{10}$$

$$\Rightarrow \begin{cases} \varepsilon'(\omega) = n^2(\omega) - k^2(\omega) \\ \varepsilon''(\omega) = 2n(\omega)k(\omega) \end{cases} \tag{11}$$

3.3.3. Optical constants

Fig. 7 shows the refractive index, n, and extinction coefficient, k, of the pure and X-doped PZT (X = Mg, Mn, and Zn) in the range of 400–700 cm^{-1}. It is clearly observed that the peak position and intensity of the n and k are shifted

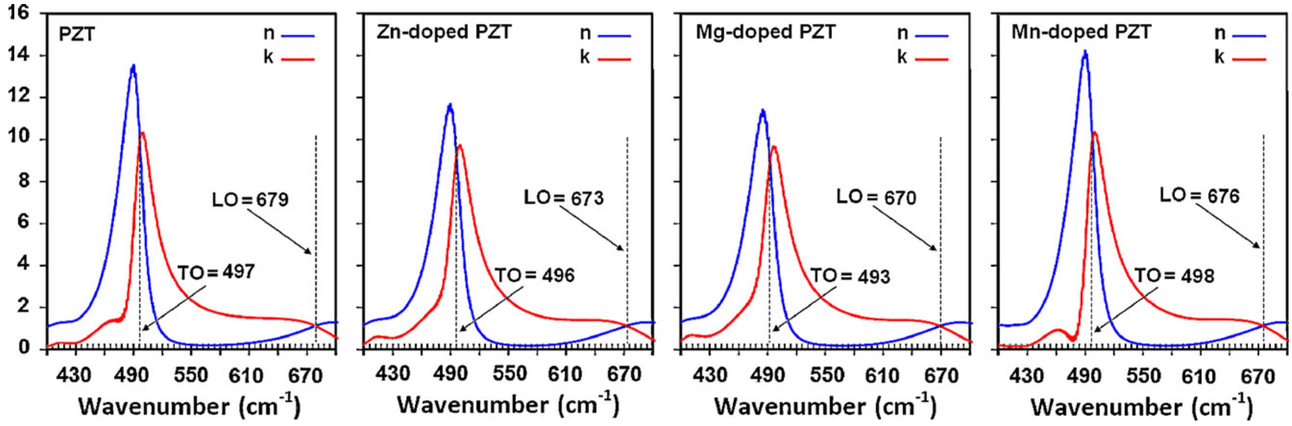

Fig. 7. The refractive index, n, and extinction coefficient, k, of pure and doped PZT-NPs in the range of 400–700 cm^{-1}. The LO and TO modes position are shown in the images.

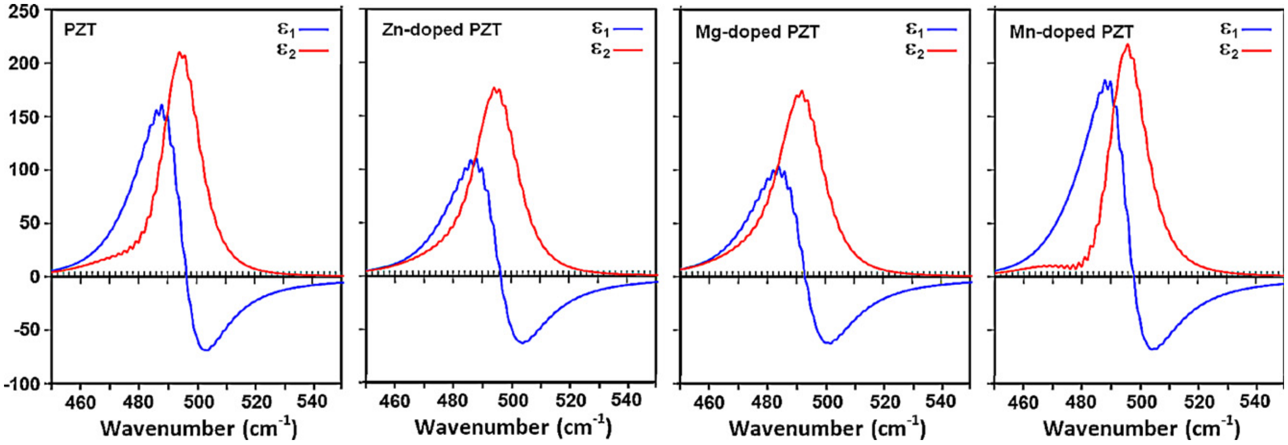

Fig. 8. The real and imaginary parts (ε_1 and ε_2) of the dielectric function of pure and doped PZT-NPs in the range of 450 cm^{-1} to 550 cm^{-1}.

significantly. The intensity of n and k peaks are decreased by substituting Ti^{4+} with Zn^{2+} and Mg^{2+} and increases with substitution Mn^{2+} due to their different ionic radii. As mentioned earlier, the ionic radii of Zn^{2+} and Mg^{2+} are bigger than Ti^{4+}, therefore their motion in the lattice is more difficult comparing to Ti^{4+}. But for Mn with smaller ionic radius, n and k peaks intensities have increased.

The real and imaginary parts of the dielectric function of pure and doped PZT-NPs are shown in Fig. 8, in which ε_1 and ε_2 are mainly in the range of 450–550 cm^{-1}. It is observed that both real and imaginary parts of the samples permittivity are decreased for Mg and Zn doped PZT-NPs, while are increased for Mn doped PZT-NPs comparing to the pure PZT-NPs. In addition, the resonance frequency of Mg and Zn doped PZT-NPs have significant red shifts, but a blue shift was observed for Mn doped PZT-NPs.

3.3.4. Optical phonon modes

The longitudinal and transverse optical phonons (LO and TO) are very useful for describing the optical interactions of light with lattice. LO and TO optical modes can be estimated from the extinction and refraction traces. As shown in Fig. 7, there are two intersection points for n and k graphs. The first point, with the lower wavenumber, is related to TO, and the second point, with the higher wavenumber, corresponds to LO mode [23]. The longitudinal and transverse optical phonons frequencies of pure and doped PZT-PNs are presented in Table 3.

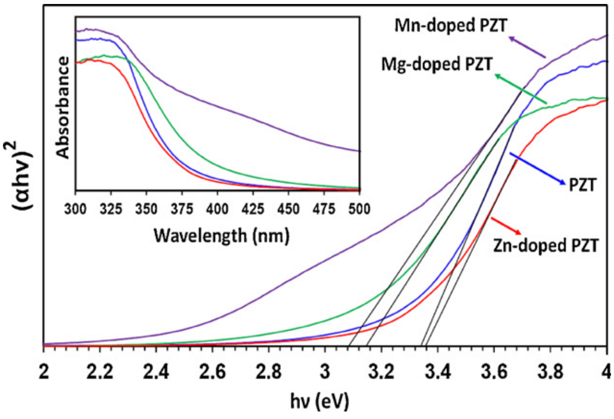

Fig. 9. Plot of $(\alpha \times h\nu)^2$ versus photon energy ($h\nu$). The inset shows the absorbance spectra of the samples.

3.3.5. UV–vis absorbance spectra

UV–vis absorbance spectra of the pure and doped PZT-NPs prepared at calcinations temperature of 700 °C are shown in the inset of Fig. 9. The relevant increase in the absorption for wavelengths less than 400 nm can be assigned to the intrinsic band-gap absorption of PZT due to the electron transitions from the valence to the conduction band because of its direct band-gap [24]. It was revealed that the optical band gap value of the PZT-NPs increases when doped with Zn cations; whereas, it is decreased when PZT-NPs were doped with Mg and Mn cations. These changes can be related to variation of the morphologies, particle size and surface microstructures of the doped PZT-NPs in comparison with undoped samples. Moreover, the direct band-gap energies can be obtained from a plot of $(\alpha \times h\nu)^2$ versus the photon energy ($h\nu$), according to Kubelka–Munk model [13]. The amount of the optical band-gap energy obtained for pure and Zn, Mg, and Mn doped PZT-NPs are 3.34, 3.36, 3.16, and 3.08 eV, respectively.

3.4. Morphology and EDX studies

Fig. 10 shows FESEM micrograph of the pure and doped PZT-NPs synthesized by sol-combustion method following with their corresponding energy dispersive X-ray (EDX) spectroscopy results. It is observed that the pure and doped PZT-NPs powders are well separated and defined in the grain size range of 50–120 nm. EDX spectroscopies confirm that the samples consist primarily of Pb, Ti, Zr, Mn, Zn, and Mg. There is no remarkable difference with the grain size detected for pure and doped PZT-NPs. This means that the growth of the PZT-NPs are not affected by the dopants, because of their low concentrations.

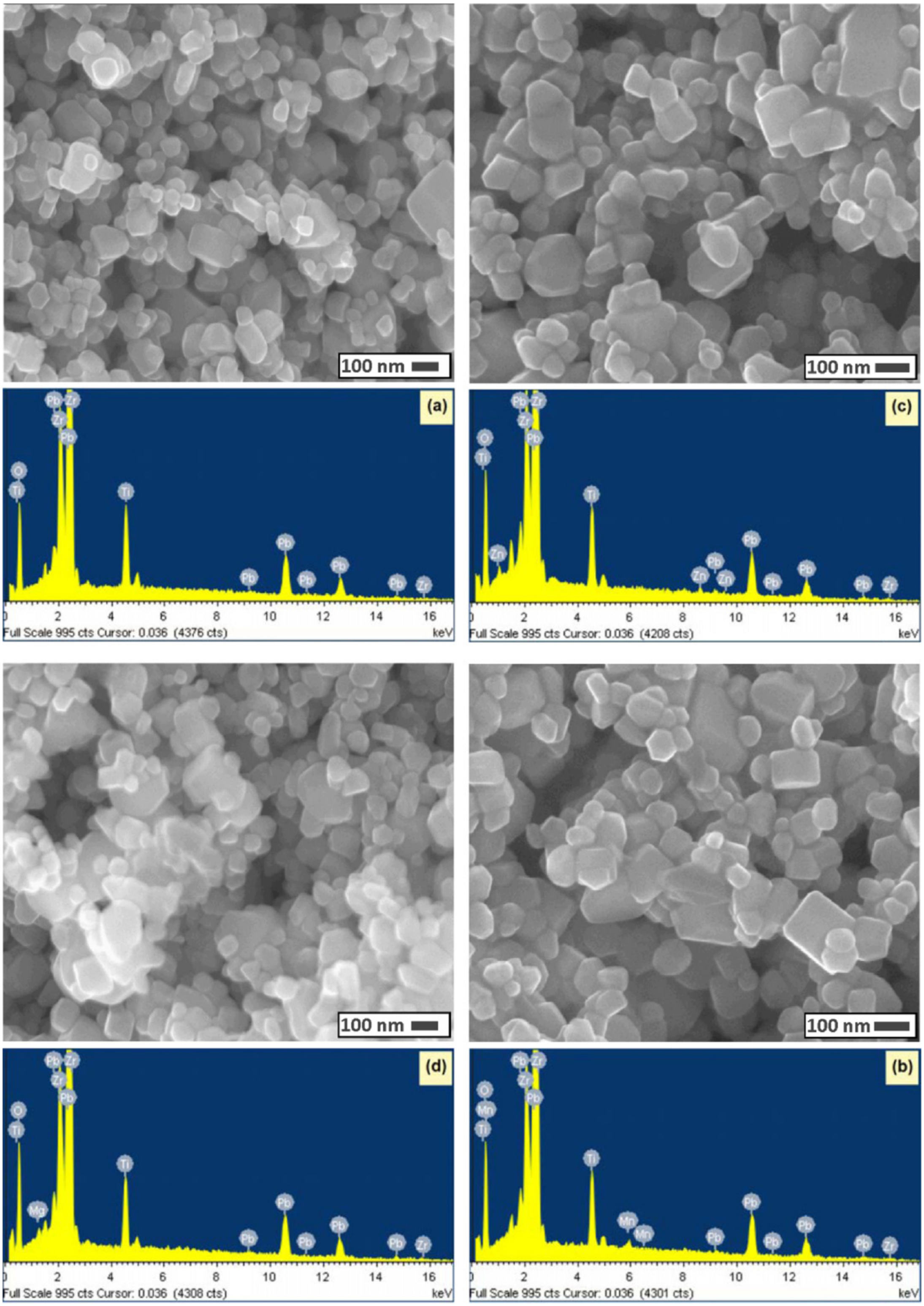

Fig. 10. FESEM micrograph and their corresponding EDX images of (a) pure PZT-NPs, (b) Zn doped-PZT-NPs, (c) Mg-doped PZT-NPs, and (d) Mn-doped PZT-NPs.

4. Conclusion

Pure and X-doped (X = Mg, Mn, and Zn) PZT-NPs were successfully prepared by sol-combustion method at calcination temperature of 700 °C. The prepared materials were characterized and investigated using XRD, FTIR, UV–vis, TEM, and EDX techniques. XRD results showed that the PZT-NPs are formed in perovskite structure with good crystallity and the crystalline sizes were found to be 94, 90, 65, 100 nm for pure and Zn, Mg, and Mn doped PZT-NPs, respectively. Phonon vibration modes of the samples were investigated using K–K relations and FTIR spectra. It was observed that the LO and TO optical phonon modes of PZT-NPs are changed between 670–679 and 493–498 wavenumber for pure and doped samples, respectively. The optical band-gap of the pure and Zn, Mg, and Mn doped PZT-NPs were estimated from UV–vis absorption results and are obtained to be 3.34, 3.36, 3.16, and 3.08 eV, respectively. From FESEM images it was revealed that the pure and doped PZT-NPs powders are well separated with the grain size in the range of 50–100 nm. EDX spectroscopy confirmed that the samples consist primarily of Pb, Ti, Zr, Mn, Zn, and Mg. The results showed that the optical properties of the PZT-NPs can be controlled by suitable dopants.

Acknowledgment

This work was suppurated by Ferdowsi University of Mashhad (Vice president for research and technology).

References

[1] W.G. Nelson, Piezoelectric Materials: Structure, Properties and Applications, Nova Science Publishers, New York, 2010.

[2] Y. Yang, Y. Hu, Y. Lu, Sensitivity of PZT impedance sensors for damage detection of concrete structures, Sensors 8 (1) (2008) 327–346.

[3] S.C. Jeffrey, K. Seung-Hyun, W. Satoshi, C. Abhijit, Characterization of Bi and Fe co-doped PZT capacitors for FeRAM, Science and Technology of Advanced Materials 11 (2010) 044402.

[4] M.-M. Zhang, Z. Jia, T.-L. Ren, Effects of electrodes on the properties of sol–gel PZT based capacitors in FeRAM, Solid-State Electronics 53 (5) (2009) 473–477.

[5] Z. Jiwei, Y. Xi, Z. Liangying, The optical waveguide characteristics of highly orientated sol–gel derived polycrystalline ferroelectric PZT thin films, Ceramics International 27 (5) (2001) 585–589.

[6] A. Khorsand Zak, W.H. Abd Majid, Characterization and X-ray peak broadening analysis in PZT nanoparticles prepared by modified sol–gel method, Ceramics International 36 (6) (2010) 1905–1910.

[7] C. Liu, B. Zou, A.J. Rondinone, Z.J. Zhang, Sol–gel synthesis of free-standing ferroelectric lead zirconate titanate nanoparticles, Journal of the American Chemical Society 123 (18) (2001) 4344–4345.

[8] M. Ghasemifard, S.M. Hosseini, A. Khorsand Zak, G.H. Khorrami, Microstructural and optical characterization of PZT nanopowder prepared at low temperature, Physica E: Low-dimensional Systems and Nanostructures 41 (3) (2009) 418–422.

[9] Y. Deng, L. Liu, Y. Cheng, C.-W. Nan, S.-j. Zhao, Hydrothermal synthesis and characterization of nanocrystalline PZT powders, Materials Letters 57 (11) (2003) 1675–1678.

[10] G. Garnweitner, M. Niederberger, Nonaqueous surfactant-free synthesis routes to metal oxide nanoparticles, Journal of the American Ceramic Society 89 (6) (2006) 1801–1808.

[11] G. Xu, G. Zhao, Z. Ren, G. Shen, G. Han, PVA assisted synthesis of nanosized perovskite PZT powder by a two-stage precipitation route, Materials Letters 60 (5) (2006) 685–688.

[12] Z. Branković, G. Branković, Č. Jovalekić, Y. Maniette, M. Cilense, J.A. Varela, Mechanochemical synthesis of PZT powders, Materials Science and Engineering: A 345 (1–2) (2003) 243–248.

[13] A.K. Zak, W.H.A. Majid, Effect of solvent on structure and optical properties of PZT nanoparticles prepared by sol–gel method, in infrared region, Ceramics International 37 (3) (2011) 753–758.

[14] J. Lappalainen, J. Hiltunen, V. Lantto, Characterization of optical properties of nanocrystalline doped PZT thin films, Journal of the European Ceramic Society 25 (12) (2005) 2273–2276.

[15] A. Khorsand Zak, R. Yousefi, W.H.A. Majid, M.R. Muhamad, Facile synthesis and X-ray peak broadening studies of $Zn_{1-x}Mg_xO$ nanoparticles, Ceramics International 38 (2012) 2059–2064.

[16] A. Khorsand Zak, W.H. Abd Majid, M.E. Abrishami, R. Yousefi, X-ray analysis of ZnO nanoparticles by Williamson–Hall and size–strain plot methods, Solid State Sciences 13 (1) (2011) 251–256.

[17] M.A. Tagliente, M. Massaro, Strain-driven (0 0 2) preferred orientation of ZnO nanoparticles in ion-implanted silica, Nuclear Instruments and Methods in Physics Research Section B: Beam Interactions with Materials and Atoms 266 (7) (2008) 1055–1061.

[18] B.D. Cullity, S.R. Stock, Elements of X-ray Diffraction, Prentice Hall, Harlow, 2001.

[19] W.G. Spitzer, R.C. Miller, D.A. Kleinman, L.E. Howarth, Far infrared dielectric dispersion in BaTiO_{3}, SrTiO_{3}, and TiO_{2}, Physical Review 126 (5) (1962) 1710–1721.

[20] D.C. Harris, M.D. Bertolucci, Symmetry, Spectroscopy and Introduction to Vibrational Electronic Spectroscopy, Dover, New York, 1978.

[21] V. Lucarini, J.J. Saarinen, K.E. Peiponen, E.M. Vartiainen, Kramers–Kronig Relations in Optical Materials Research, Springer, Berlin, Heidelberg, New York, 2004.

[22] M. Ghasemifard, S.M. Hosseini, G.H. Khorrami, Synthesis and structure of PMN–PT ceramic nanopowder free from pyrochlore phase, Ceramics International 35 (7) (2009) 2899–2905.

[23] S.S. Ng, Z. Hassan, H. Abu Hassan, Kramers–Kronig analysis of infrared reflectance spectra with a single resonance, Jurnal Teknologi 44 (2006) 67–76.

[24] J. Baedi, S.M. Hosseini, A. Kompany, The effect of excess titanium and crystal symmetry on electronic properties of $Pb(Zr_{1-x}Ti_x)O_3$ compounds, Computational Materials Science 43 (4) (2008) 909–916.